


ORIGINAL ARTICLE

Open Access



Core–shell CoN@Co ultra-stable nanoparticles on biochar for contamination remediation in water and soil

Qiang Yang^{1,2}, Peixin Cui^{1,2*} , Cun Liu¹, Guodong Fang¹, Fei Dang¹, Pengsheng Wang³, Shaobin Wang⁴ and Yujun Wang^{1,2}

Abstract

Nanomaterials have been extensively employed in various applications over the past several decades, however, the stability of functional nanoparticle catalysts (NPCs) for effective degradation of organic contaminants remains a significant challenge. Herein, we present a cost-effective biochar loaded uniformly dispersed ultra-stable Co nanoparticles with an average diameter of 8 nm as a highly efficient peroxymonosulfate (PMS) activation catalyst. The reactive radicals produced from the catalyst/PMS system are able to degrade several model organic pollutants of environmental and public health concerns, including trichlorobiphenyl, bisphenol A and diethyl phthalate, with less pH limitation and Co²⁺ leaching. Mechanism investigation demonstrates that the CoN plays the key role in the catalyst stability and PMS activation via acid resistance and electron bridging effects, respectively. Meanwhile, the incorporation of nitrogen (N) and sulfur (S) atoms within the substrate is considered to bolster the adhesion strength between metal nanoparticles and the carbon matrix via strong metal-support interaction. The catalyst was further applied in practical treatment of water and soil polluted by organic pollutants, exhibiting a satisfactory degradation efficiency (> 90% in 60 min) for environmental applications.

Highlights

- Homogeneous diffusion attributed to doped N/S atoms via metal-support interaction.
- Superior catalytic capability and strong stability mechanism of coated CoN.
- Extraordinary activity for peroxymonosulfate activation to degrade organic pollutants in natural water and soil.

Keywords Soil pollution remediation, Ultra-stable nanoparticle catalysts, Organic contaminants degradation, Advanced oxidation process

Handling Editor: Baoshan Xing.

*Correspondence:

Peixin Cui

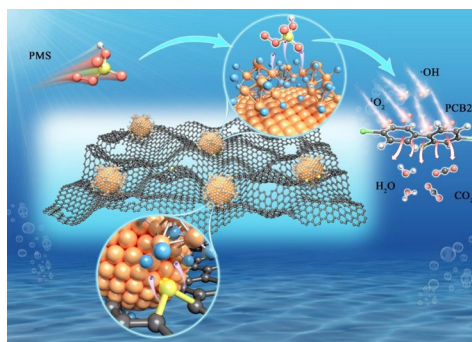
pxcui@issas.ac.cn

Full list of author information is available at the end of the article



© The Author(s) 2024. **Open Access** This article is licensed under a Creative Commons Attribution 4.0 International License, which permits use, sharing, adaptation, distribution and reproduction in any medium or format, as long as you give appropriate credit to the original author(s) and the source, provide a link to the Creative Commons licence, and indicate if changes were made. The images or other third party material in this article are included in the article's Creative Commons licence, unless indicated otherwise in a credit line to the material. If material is not included in the article's Creative Commons licence and your intended use is not permitted by statutory regulation or exceeds the permitted use, you will need to obtain permission directly from the copyright holder. To view a copy of this licence, visit <http://creativecommons.org/licenses/by/4.0/>.

Graphical Abstract



1 Introduction

Nanoparticle catalysts (NPCs) are widely applied in environmental pollution remediation. A decreased size particle is able to enhance catalytic performance significantly (Tyo and Vajda 2015; Roldan Cuenya and Behafarid 2015; Lei et al. 2010), resulting from the strong quantum size effects, increased metal atom utilization (Corma et al. 2013), and the ability to regulate electronic structures and chemical interactions between metal atoms and substrate materials (Liu and Corma 2018; Xu et al. 1994). During the synthesis, metal species tend to aggregate into larger particles due to a dramatic increase in specific surface energy with a reduced particle size (Joo et al. 2009; Dai et al. 2018). Additionally, the desired high activity of the surface structure may be destroyed in the storage or reaction processes, as unsaturated metal atoms at the surface are susceptible to oxidation or hydration (Li et al. 2020). These inherent behaviors inevitably lead to the loss of active sites and catalyst deactivation. Thus, there is an urgent need to develop preparation strategies of NPCs for establishing and maintaining stable spatial arrangements of a metal in substrates at a nanoscale.

A prevalent strategy for preparing NPCs involves loading metal nanoparticles onto a solid substrate with a high surface area (Ou et al. 2020; Li et al. 2020; Wang et al. 2022a). Carbon-based materials, particularly nitrogen (N)-doped graphite, serve as excellent substrates for NPCs due to their large specific area and the controllable interaction between the substrate and the metal nanoparticles (Jin et al. 2021). For instance, Previous study (Han et al. 2020) encapsulated cobalt (Co) nanoparticles with an average diameter of 30–50 nm in carbon nanotubes and observed that the strong interaction between the N-doped substrate and the Co nanoparticles enhanced catalytic performance. Similarly, the uniformed encapsulation of Co nanoparticles (~10 nm) in N-doped hollow carbon materials can develop a Co-pyridinic N moiety, which not only alleviates

aggregation behavior but also modulates the electron density of Co species, thereby increasing peroxymonosulfate (PMS) adsorption and conversion efficiency (Li et al. 2021b). While Co-based catalysts exhibit the highest activity for PMS activation, there are significant disadvantages, such as secondary metal contamination owing to Co²⁺ leaching (Jiang et al. 2022), low PMS utilization rate, poor structural stability, and difficult separation for reutilization. Additionally, hydrogen ions (H⁺) would be released in the reaction of PMS activation, resulting in a strong requirement of acid resistance for NPCs.

The coordination environment, facilitated by a suitable substrate, significantly influences the dispersibility, stability, and catalytic performance of NPCs (Hu and Li 2021). Previous study reported that strong chemical/electronic interactions between platinum (Pt) nanoclusters (~1 nm) and S atoms in a carbon-based substrate effectively suppressed metal aggregation by hindering metal atom diffusion and nanoparticle migration during a high-temperature catalytic reaction (Yin et al. 2021). Therefore, the substrate should generate adequate coordination species and “adhesion strength” sites, such as N, P, O and S-C bonds, to capture metal nanoparticles to stabilize NPCs. Rational designs, including NP size and metal-support interaction (MSI), are crucial for both the catalyst performance and the stability of NPCs (van Deelen et al. 2019).

Heterogeneous catalysts are typically prepared via pyrolysis of pure mononuclear metal complexes, such as metal–organic frameworks (MOFs), covalent-organic frameworks (COFs), and their derivatives (Falcaro et al. 2016; Wang and Astruc 2020). However, the complex preparation process and the high cost of precursor materials limit industrial scale applications. Few studies on NPCs have explored the use of low-cost domestic waste as precursor materials for loading transitional metal nanoparticles. Our previous work demonstrated that coffee

grounds, a common domestic waste in daily life, contain abundant N and S species and may serve as a promising alternative N/S-doped substrate (Cui et al. 2021).

This study aims to demonstrate an environmental-friendly and cost-effective NPC with a superlative stability and catalytic activity in advanced oxidation processes (AOPs) for degradation of organic pollutants in soil and water. Polychlorinated biphenyls (PCBs) as a type of persistent organic pollutant commonly detected in the top soil of industrial areas were examined, with 2,4,4'-trichlorobiphenyl (PCB28) as a representative. In this work, 2,4,4'-trichlorobiphenyl (PCB28), bisphenol A (BPA), and diethyl phthalate (DEP) were chosen as the model pollutants because of their refractory (Fang et al. 2017) and different properties (Yang et al. 2022; Guo et al. 2022). The intrinsic characteristics, catalytic mechanism and practical applications were systematically investigated and the results would benefit the development and application of low-cost NPCs for contaminant remediation in water and soil.

2 Materials and methods

2.1 Chemicals and materials

Cobalt chloride hexahydrate ($\text{CoCl}_2 \cdot 6\text{H}_2\text{O}$), nickel chloride (NiCl_2), and copper chloride (CuCl_2) were purchased from Aladdin Group Chemical Reagent Co., Ltd. (China). Potassium peroxydisulfate (99.5%), 2,4,4'-trichlorobiphenyl (PCB28, 99.5%), bisphenol A (BPA, >97%) and diethyl phthalate (DEP, 99%) were provided by Alfa Aesar Co., Inc. (China). 5,5-Dimethyl-1-pyrroline-N-oxide (DMPO) and 2,2,6,6-tetramethyl-4-piperidone hydrochloride (TEMP) were purchased from Dojindo Laboratories, Kumamoto (Japan). Inorganic salts, p-phthalic acid (PTA), 2-hydroxyterephthalic acid, humic acid (HA), ethanol (EtOH), tertbutyl alcohol (TBA) and furfuryl alcohol (FFA) were obtained from Sigma-Aldrich. All the chemicals were used without further purification. Ultrapure water from Milli-Q apparatus (Millipore, USA) was used in the experiments.

2.2 Synthesis of NPCs

Spent coffee grounds (CG, 3 g) were mixed with 40 mL of aqueous solution containing 4.24 mM Co^{2+} at ambient temperature (25 °C) and stirred at 200 rpm for 24 h. The adsorbed CG was separated via centrifugation (5000 rpm, 10 min) and dried in an oven at 80 °C overnight. The resulting solid was pyrolyzed at 600, 700, and 900 °C for 4 h at a heating rate of 1 °C·min⁻¹ in a tube furnace with high-purity N_2 atmosphere at a flow rate of 20 mL·min⁻¹. The resulting black powder was named Co-CGBC-600, Co-CGBC-700, and Co-CGBC-900, respectively. For comparison, the material obtained by treatment of CG powder under the same conditions in the absence of Co^{2+} was named CGBC. In addition, Ni-CGBC-700 and

Cu-CGBC-700 were prepared by the same procedure as Co-CGBC-700, with Co^{2+} replaced by Ni^{2+} and Cu^{2+} .

2.3 Characterizations

The concentration of dissolved Co^{2+} in the acid treatment was measured via Inductively Coupled Plasma Optical Emission Spectrometry (ICP-OES). The obtained NPCs were characterized by X-ray diffraction (XRD, Rigaku Ultima IVI, Japan), scanning electron microscopy (SEM, Genimi500, USA), high-resolution transmission electron microscopy (HR-TEM, jem-2100F, JEOL, Japan), TG-IR analysis (Mettler-Toledo TG2 + Nicolet iS50, Thermo Fisher Scientific, Japan), X-ray photoelectron spectroscopy (XPS, Thermo VG ESCALAB 251XI) and X-ray absorption fine structure spectroscopy (XAFS).

2.4 Catalytic degradation

The batch experiments were employed to investigate the catalytic performance of Co-CGBCs. The degradations of PCB28, BPA and DEP were evaluated under different conditions, including varying dose of catalyst, concentration of PMS, pH, and coexisting ions. The recycle performance of catalysts were investigated under optimal conditions, collected with an external magnetic field. The catalytic performance in actual contamination water and soil was also studied for practical application. The details are listed in Text S1.

2.5 Mechanism investigation

Electron paramagnetic resonance (EPR, Bruker E580 spectrometer, Germany) was conducted to identify the main reactive oxygen species (ROs) generated in the catalytic process. The details of density functional theory (DFT) calculations are listed in Text S2.

3 Results and discussion

3.1 Characterizations of Co NPs

The X-ray diffraction (XRD) patterns (Fig. S1a) for pure CGBC-700 exhibited two broad peaks located at 23.6° and 43.1°, which were assigned to the amorphous carbon peak. By contrast, the sharp peaks located at 42.7°, 44.1°, and 51.3°, corresponded to the characteristic peaks of CoN and metallic Co, respectively (Fig. S1b). The elemental contents of the prepared materials are listed in Table S1. The thermal stability and binding phenomena were revealed by TG-IR analysis (Fig. S2). The mass loss ratio of biomass was up to 77.7% and the intensities of C=C, C=O, C≡C, and C≡N in Co-CGBCs were more evident than that of CGBCs during the pyrolysis process, implying that the existence of metal NPs could affect the chemical properties and structure of carbon substrate. The Brunner-Emmet-Teller (BET) results and pore size distribution of Co-CGBC-700 are displayed in Fig. S3

and Table S2. The micropore area ($67.53 \text{ m}^2 \text{ g}^{-1}$) was far larger than external surface area ($8.81 \text{ m}^2 \text{ g}^{-1}$), suggesting that Co-CGBC-700 exhibited an advanced micropore structure. The SEM was employed to examine the porous morphology of Co-CGBC-700 (Fig. 1a). The HR-TEM images revealed high crystallinity core-shell structure in Co-CGBC-700, where metallic Co(102)/CoS(102) was coated by CoN(200) and CoN(111) lattice fringes, with d -spacing of 0.192, 0.214 and 0.245 nm (Guo et al. 2018), respectively (Fig. 1b and S4), in accordance with the magnetic separation and leaching tests (Fig. S5). Moreover, HR-TEM elemental line scanning and elemental mapping analysis showed that the location of S and Co overlapped significantly (Fig. 1c, d), indicating the strong relationship between the Co and S. All these results imply that Co/CoS nanoparticles are covered with CoN and anchored by strong metal-substrate interaction, enhancing both acid resistance and aggregation in Co-CGBC-700 (Song et al. 2019). Co nanoparticle sizes in Co-CGBCs varied with different pyrolysis temperatures. The average size of nanoparticles in Co-CGBC-700 was $8.5 \pm 1.4 \text{ nm}$ (Fig. 1e), while they sharply increased to 20–100 nm in Co-CGBC-900 (Fig. S6). These findings imply that, at high pyrolysis temperatures, the metal-substrate connection was disrupted, resulting in uncontrolled aggregation. The particle size in Co-CGBC-700 remained nearly constant ($8.3 \pm 1.0 \text{ nm}$) after acid treatment in 1 M H_2SO_4 (Fig. S7), with a leaching rate of $\sim 2\%$ (Fig. S5).

Surface-sensitive XPS measurements were conducted to better understand the surface chemical environment (the C 1 s, N 1 s, S 2p, and Co 2p core levels of atoms)

by determining the binding energy and the chemical state of the material's surface (Kigozi et al. 2020; Moses et al. 2023). The full-spectrum scan of XPS and C 1 s XPS deconvolution are displayed in Fig. S8. The N 1 s and S 2p deconvolution of Co-CGBC-700 are shown in Fig. 2a, b, the peaks at 397.7 and 164.7 eV correspond to N-Co and S-Co bonding energies (Wang et al. 2019), respectively. A noticeable fitting peak emerged from the N-Co bond in Co-CGBC-600 and Co-CGBC-700, but the intensity of this peak significantly weakened in Co-CGBC-900, suggesting that the Co-N bonding in the Co NPs was reduced at the highest pyrolysis temperature (Figs. S9 and S10). Based on the study of the N and S XPS spectra, it was proven that Co had a dynamic binding environment, with Co-N-C gradually changing into Co-S-C as the pyrolysis temperature rose. The Co 2p XPS of Co-CGBC-700 is shown in Fig. S11 and could be deconvoluted into eight peaks, while two fitting peaks of Co 2p_{3/2} located at 780.4 eV and 782.0 eV were attributed to Co(II) and Co-N_x, respectively (Yang et al. 2019). The presence of Co-N_x is beneficial for the stabilization of Co NPs, as previously mentioned.

Synchrotron-based XAFS was employed to further investigate the atomic and electronic structure behavior of Co-CGBCs. As displayed in Fig. 2c, the N K-edge near edge X-ray absorption fine structure (NEXAFS) spectrum of Co-CGBC-700 exhibits sharp peaks corresponding to transitions from 1 s to π^* orbitals and a broad peak corresponding to σ^* resonance. The sharp π^* peaks could be split into four distinct peaks at 397.0, 398.4, 399.7 and 401.5 eV, assigned to N-Co, pyridine N,

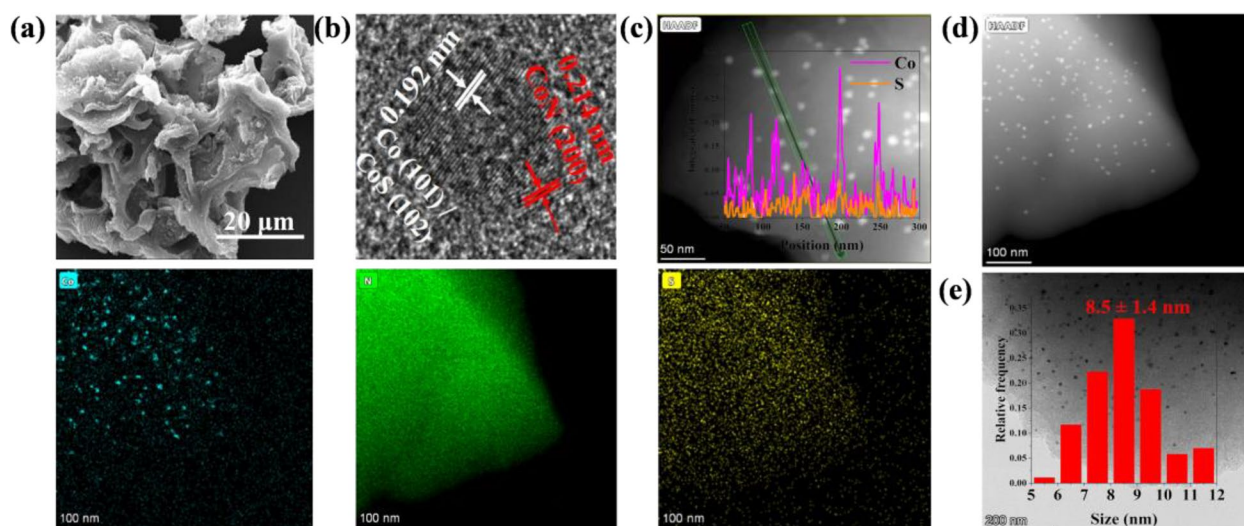


Fig. 1 a SEM image of Co-CGBC-700, b the interlayer spacing of Co(101) or CoS(102) and CoN(200), c S/Co atomic fraction determined by HR-TEM elemental line scanning analysis, d elemental mapping of Co-CGBC-700, Co (light blue), N (green), and S (yellow), e size distributions of Co NPs in carbon matrix

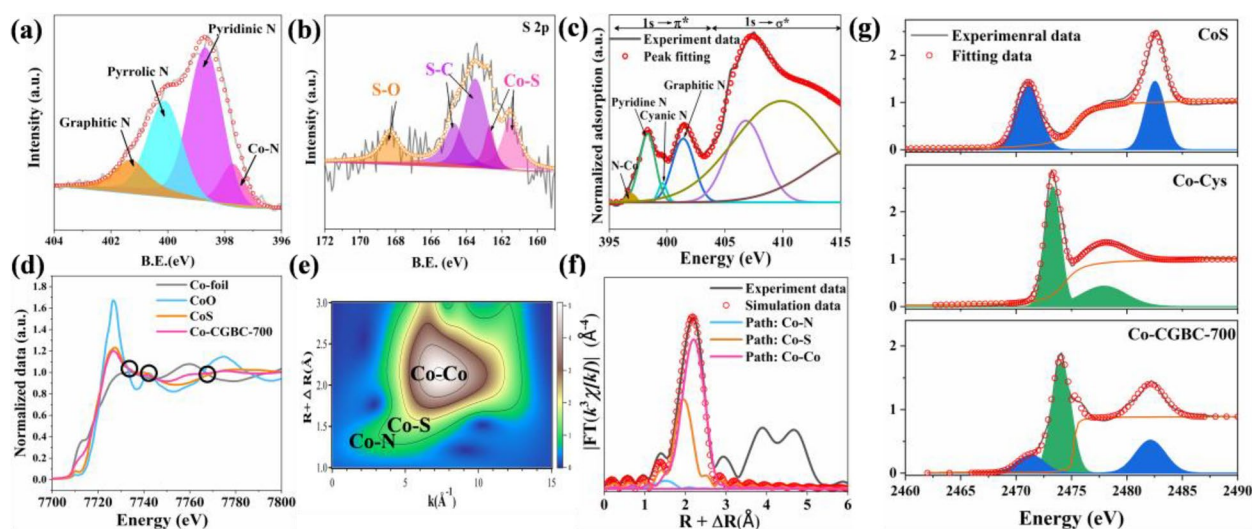


Fig. 2 a, b N 1s and S 2p XPS spectra of Co-CGBC-700, c NEXAFS spectra of Co-CGBC-700 at N K-edge, d the normalized Co K-edge XAFS spectra, e the corresponding WT-EXAFS plot of and f NEXAFS spectra and peak fitting of Co-CGBC-700, g NEXAFS spectra of Co-CGBC-700 and references at S K-edge

cyanoic N and graphite N, respectively. This result proves once again that Co–N bonding is present at the surface of Co NPs. In the S K-edge NEXAFS spectrum (Fig. 2g), the doublet peaks located at 2470–2475 eV could be deconvoluted into two peaks at 2471.1 and 2473.3 eV, which are the same positions as the characteristic peaks in the reference spectra of CoS and cysteine, confirming the presence of C–S–Co coordination and suggesting that S atoms play a key role in the anchoring of Co NPs.

The chemical species of Co of Co-CGBCs were established by Co K-edge XAFS. The normalized spectra of Co-CGBC-700 and Co foil, CoO and CoS references are shown in Fig. 2d. The absorption edge of Co-CGBC-700 was located between that of Co foil and CoS, indicating that the main species in the Co-CGBC-700 may be a mixture of metallic Co and CoS at the nanoscale. Notably, the spectra of Co-CGBC-700, Co foil and CoS share several isobestic points (black circles in Fig. 2d), confirming that Co-CGBC-700 was a mixture of metallic Co and CoS (Wu et al. 2019). The wavelet-translated (WT) extended X-ray absorption fine structure (EXAFS) spectra of Co-CGBC-700 and the references were obtained with high resolution in both the k and R spaces (Fig. 2e and S12). The main WT peak at $\sim 7.5 \text{ \AA}^{-1}$ could be attributed to Co–Co coordination, according to the WT pattern of Co foil. There were two minor peaks at ~ 6.0 and $\sim 4.7 \text{ \AA}^{-1}$, which could be identified as Co–S and Co–N coordination, respectively, based on the WT patterns of CoS and CoO. The fitting of the Fourier-transformed EXAFS spectra for the Co-CGBCs and the references are displayed in Fig. 2f, S13 and S14, and the local structural parameters

are listed in Table S3. There were three separate peaks in Co-CGBC-700, which arose from Co–N, Co–S and Co–Co coordination. The coordination numbers of Co to N, S and Co were 0.5, 1.6 and 8.6, respectively, which suggests that Co NPs were consisted of 71% metallic Co, 26% CoS and trace CoN, on the basis of the coordination numbers of Co–Co bonds in Co foil and Co–S in CoS. The N, S and Co XAFS further confirmed the core–shell structure of CoN@Co/CoS, consistent with the HR-TEM and XPS results.

3.2 Mechanism investigation of homogeneous distribution

Density functional theory calculations were carried out to explore the possible mechanisms of homogeneous distribution and to elucidate the critical role of the interfacial N and S–C bonds in metal nanocluster sintering during the high-temperature pyrolysis process (DFT calculation in Text S2). Based on the geometric structural details identified in the HR-TEM images (Fig. 1b and S4), the small Co cluster (Co_{36}) in the shape of truncated octahedron with exposed $\text{Co}101$ planes were proposed for the surfaces of N-doped, S-doped and N/S co-doped graphene models for the first examination with DFT (Fig. 3a, b and c). A defect-free graphene layer was also included for comparison (Fig. 3d). The Co_{36} clusters were anchored on biochar surface defects through Co–S or Co–N bonds, with average bond lengths of 2.24 and 2.09 \AA , respectively, while the closest distance between Co clusters and perfect graphene was 3.73 \AA , which is similar to the coordination environment of Co-CGBC-700 based on the HRTEM, XPS and XAFS analyses.

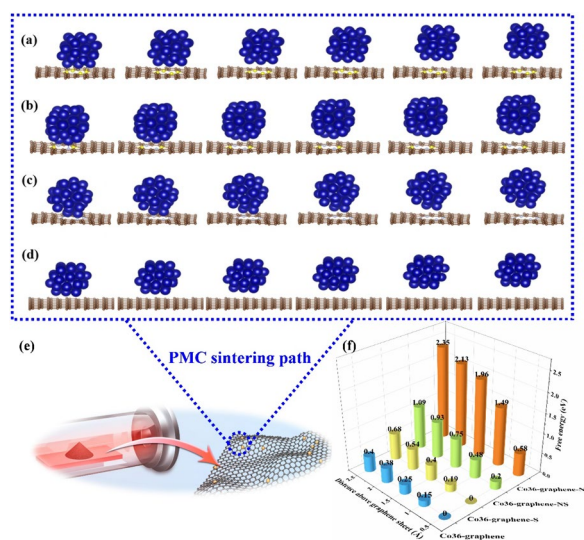


Fig. 3 DFT simulation of the Co₃₆ nanocluster desorbed from **a** S-doped graphene, **b** N, S-doped graphene, **c** N-doped graphene, and **d** pristine graphene, **e** diagram of particle migration and coalescence (PMC) sintering path during the pyrolysis process, **f** energy required for Co nanocluster to be desorbed from the different substrates

For the simulation, we calculated the particle migration and coalescence (PMC) sintering path during the high-temperature pyrolysis process (Fig. 3e). The PMC sintering mechanism involves the mobility of whole particles on the substrate with Brownian motion collisions (Hansen et al. 2013). Thus, the migration trends of a Co₃₆ particle could be inferred according to the adhesion strength of the metal-graphene. As shown in Fig. 3f, DFT calculations showed a much higher energy barrier for the Co₃₆ nanocluster desorption from N-doped graphene (0.55 eV) than those on N/S co-doped graphene, S-doped graphene and the defect-free graphene surface (0.12, 0.02, and 0.01 eV, respectively). This indicates that the PMC process can be significantly suppressed for Co nanoclusters on N-doped or N, S-co-doped substrates. With increased distances, the free energy of Co nanoclusters for diffusion increased as well, and the values of free energy followed the order of Co₃₆-graphene N (2.19 eV) > Co₃₆-graphene NS (0.86 eV) > Co₃₆-graphene S (0.60 eV) > Co₃₆-graphene (0.27 eV). This suggests that the stronger bonding of Co–N contributes to a higher energy penalty for the small Co clusters moving away from adsorption sites to form larger aggregates by hindering the PMC path (Dai et al. 2018), which may be the main mechanism of the homogeneous distribution of NPs on the carbon substrate surface.

3.3 Superlative catalytic activities towards AOPs

In the batch experiments, PCB28 was barely degraded by PMS, CGBC-700 substrate and Co-CGBC-700. Approximately 70% of PCB28 decomposed within 10 min after

PMS injection at pH 6.5 in the presence of Co-CGBC-700 (Fig. 4a), indicating that Co-CGBC-700 exhibits superlative catalytic performance in PMS activation. The consumption of PMS was quantitatively probed using KI (Fig. S15), and more than 75% of PMS was consumed in the initial 5 min, confirming the superlative catalytic activities of Co-CGBC-700. In a homogeneous system with the equivalent amount of Co²⁺ (14.5 mg·L⁻¹ based on Table S1), 53.2% PCB28 was removed, indicating that the incorporation of N-coordinated NPCs resulted in higher activities.

The catalytic performances of Co-CGBCs obtained at different annealing temperatures were also compared, and the time-course data were fitted by a pseudo-first-order kinetic model for the initial 30 min of reaction. The rate constant (k_{obs}) values followed the order of Co-CGBC-900 (0.0461 min⁻¹) > Co-CGBC-700 (0.0403 min⁻¹) > Co-CGBC-600 (0.0261 min⁻¹) (Fig. 4b) and the final removal rate of PCB28 at 83.4% was achieved by Co-CGBC-700/PMS system. More importantly, the dissolution concentrations of Co²⁺ for Co-CGBC-600, -700 and -900 after the reaction were 0.05, 0.07 and 2.15 mg L⁻¹, respectively. The inferior catalytic performance of Co-CGBC-600 during the PCB28 degradation process may be attributed to the low graphitization degree of the carbon skeleton, as most PCB28 molecules cannot be adsorbed and concentrated on pyrrolic N moieties in an amorphous carbon matrix (Fig. S16). This would severely hinder the mass transfer course and extend the migration distance of the ROSs produced from PMS activation, thus reducing the Fenton-like catalytic performance (Xiong et al. 2022). In comparison, Co-CGBC-700 exhibited a more ordered graphitic structure adjacent to the NPCs site (Fig. S4), which not only promoted the catalytic performance but also produced a beneficial effect to the stability of the NPCs (Gao et al. 2021; Li et al. 2018).

The stability and reusability of Co-CGBC-700 were assessed through a minimum of three consecutive trials under similar conditions. The catalyst was separated using an external magnetic field and rinsed with N-hexane and deionized water in each trial. As shown in Fig. 4c, Co-CGBC-700 maintained exceptional degradation performance in three cycles, with a degradation efficiency of approximately 80%. The Co²⁺ leaching concentration remained below 0.07 mg L⁻¹ in solution after each reaction, significantly lower than the acceptable limit of 1 mg L⁻¹ as defined by the Chinese National Standard (GB 25467–2010). Considering the overall performance and leaching concentration of Co²⁺, Co-CGBC-700 can be considered to be the most promising catalyst.

To evaluate the practical applicability of Co-CGBC-700 under environmental conditions, we investigated the

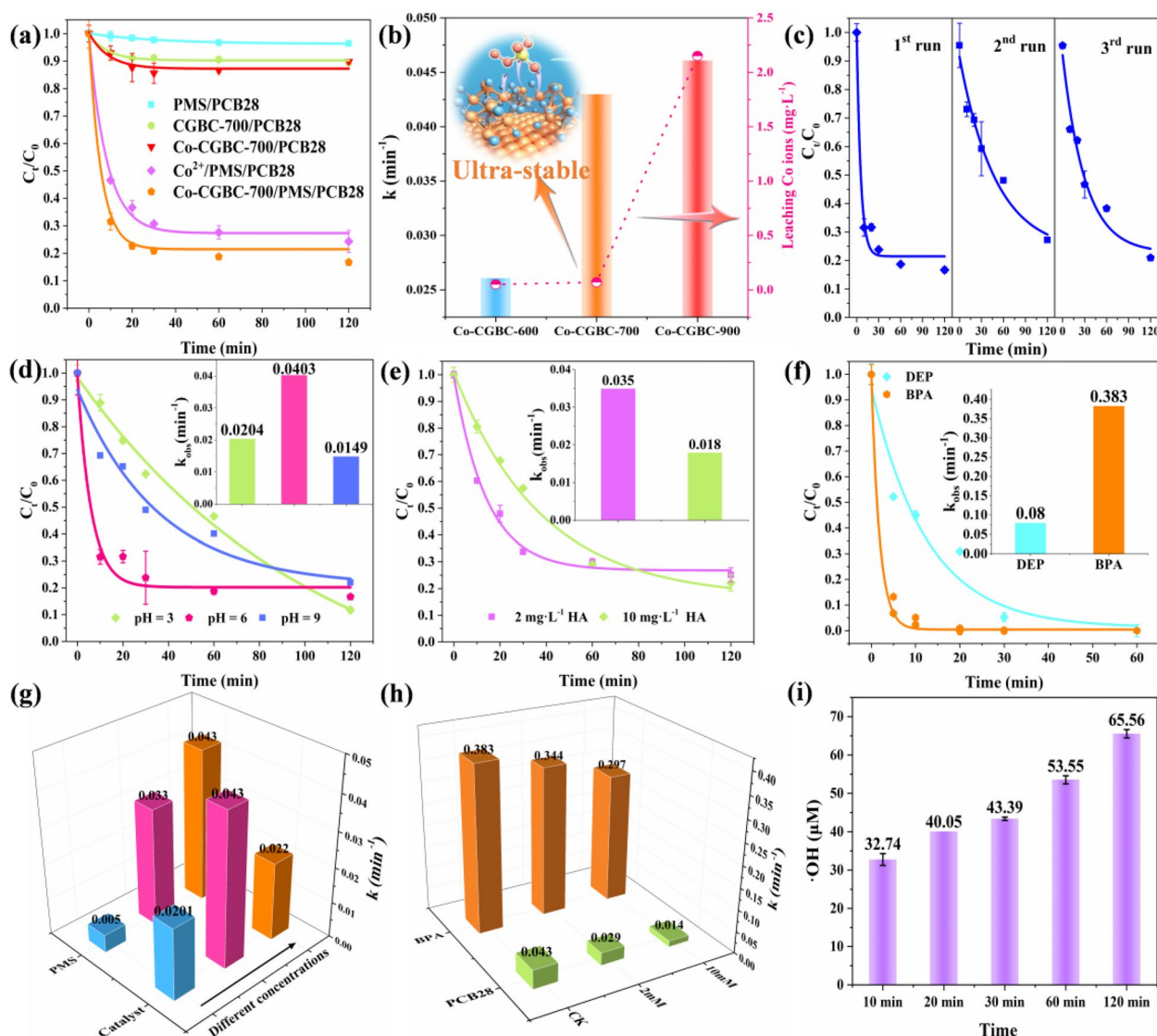


Fig. 4 **a** Kinetics of PCB28 degradation by PMS alone, CGBC-700, Co-CGBC-700, and equivalent Co²⁺, **b** catalytic activity for Co-CGBC-x (x stands for different pyrolysis temperature) and the corresponding concentrations of leaching Co ions, **c** evolution of catalytic activity in Co-CGBC-700/PMS system after three cycles, **d** influence of pH, and **e** HA on PCB28 degradation, **f** catalytic activity for different organic pollutants, **g** effect of different catalyst dosages and PMS concentrations, **h** effect of different concentrations of TBA on PCB28 and BPA degradation, **i** the yield of ·OH in Co-CGBC-700/PMS system using PTA as a molecular-probe. [Catalyst] = 1.0 g·L⁻¹, [PMS] = 2 mM, [PCB28] = 2 mg·L⁻¹, [BPA, DEP] = 100 mg·L⁻¹, pH = 6.5, [PTA] = 2 Mm

catalytic performance at varying pH levels, catalyst doses, PMS concentrations, and the presence of coexisting anions (Bao et al. 2022). As displayed in Fig. 4d and Text S3, the degradation rates of PCB28 at pH levels of 3, 6 and 9 were 78%, 84%, and 89% within 120 min, respectively. Notably, the optimal catalytic performance was achieved under weak acid conditions. The influence of varying Co-CGBC-700 dosages on PCB28 degradation is depicted in Fig. 4e and S17a. The PCB28 removal efficiency increased from 55.2% to 84% as the catalyst dosage rose from 0.5 to

1.0 g L⁻¹, which was anticipated to be due to the increased availability of active sites. However, the removal rate decreased to 63.4% when the dosage increased to 1.5 g L⁻¹, potentially attributed to the rapid consumption of PMS and the self-quenching reaction among radicals (Chen et al. 2019). The PCB28 degradation rate was also investigated at different PMS dosages (Fig. 4e and S17b), revealing an increase from 36.5% to 84% as PMS concentration increased from 0.5 to 2.0 mM, indicating that PMS dosage was the key rate limiting factor.

In the presence of naturally occurring anions, such as Cl^- and HCO_3^- , the degradation rates dropped to less than 40% at a high concentration (10 and 20 mM) but were less affected at a lower anion concentration of 5 mM (Fig. S17c and d), indicating the wide applicability of the method. Cl^- could scavenge ROSs and form halogen species (Cl^\bullet , $\text{Cl}_2^{\bullet-}$ and $\text{ClOH}^{\bullet-}$), which were incapable to degrade PCB28, suggesting the significant inhibition of Cl^- on PCB28 degradation in Co-CGBC-700/PMS system. Comparing with Cl^- , the addition of HCO_3^- did not change the PCB28 degradation rate significantly. The low concentration of HCO_3^- may directly complex with Co sites to form unreactive cobalt-bicarbonate complexes but PMS could be activated by the rest of Co sites (Duan et al. 2018). The impact of natural organic matter (NOM) was examined using humic acid (HA) as a representative compound (Duan et al. 2018). With the presence of 2 and 10 mg L^{-1} HA, the PCB28 degradation rates were maintained at 80% (Fig. 4f and Text S4), signifying a negligible inhibitory effect of NOM.

In addition, two other organic pollutants (DEP and BPA) were used to investigate the wide applicability of Co-CGBC-700. Both pollutants were completely degraded within 30 min (Fig. 4g). The k_{obs} of BPA was significantly larger than that of DEP, suggesting that the primary degradation mechanisms for these contaminants were different. BPA, possessing an electron-donating group (-OH), would be governed by a non-free radical degradation pathway, such as electron transfer, high-valence metals and single oxygen ($^1\text{O}_2$), while DEP, containing an electron-withdrawing group (-COO-, -CH₃), would primarily undergo a radical oxidation process (Yang et al. 2022; Guo et al. 2022). Consequently, Co-CGBC-700 exhibited an excellent catalytic performance in PMS activation to degrade various organic pollutants. In comparison, we also summarized the current and relevant literatures (Table S4) to show the excellent catalytic performance of Co-CGBC-700.

3.4 Catalytic mechanism investigation

The activation process of PMS generally encompasses radical or non-radical oxidation pathways (Zhang et al. 2021). Both DEP and PCB28 have an electron-donating group (-COO-, -CH₃, Cl^-), suggesting that they may primarily undergo a similar degradation pathway (radical oxidation process). Therefore, free radical trapping and quenching experiments were conducted to confirm the assumptions. ROSs in the Fenton-like catalysis were verified by electron paramagnetic resonance (EPR) with 5,5-dimethyl-1-pyrroline (DMPO) and 2,2,6,6-tetramethylpiperidine (TEMP) as the spin-trapping reagents (Wang et al. 2022b; Wu et al. 2021).

As shown in Fig. S18a, with the presence of Co-CGBC-700, no discernible free radical signals such as

DMPO- $\bullet\text{OH}$ and DMPO- $\text{SO}_4^{\bullet-}$ were observed. While the characteristic of seven-line signals with $\alpha_{\text{N}}=7.2\text{G}$ and $\alpha_{\text{H}}^{\text{r}}=4.1\text{G}$ were identified as 5,5-dimethyl-2-pyrrolidone-*N*-oxyl (DMPOX) (Li et al. 2021a), generated via direct oxidation of DMPO by $^1\text{O}_2$ (Li et al. 2015). Furthermore, intense characteristic triplet signals of $^1\text{O}_2$ were observed in the Co-CGBC-700/PMS system when trapped by TEMP (Fig. S18b), clearly demonstrating that $^1\text{O}_2$ is an active species in the Fenton-like reaction (Yao et al. 2022). Moreover, the yield of $\bullet\text{OH}$ was quantitatively monitored using PTA as the molecular probe (Fig. 4h), with the accumulated concentration of $\bullet\text{OH}$ reaching 65.56 μM throughout 120 min reaction (Kilic et al. 2019). Consequently, $\bullet\text{OH}$ could be involved in the PCB28 degradation process, despite the absence of DMPO- $\bullet\text{OH}$ in EPR analysis. The lack of DMPO- $\bullet\text{OH}$ and DMPO- $\text{SO}_4^{\bullet-}$ generation may be attributed to the difficulty in trapping the surface-bound radicals by DMPO (Zhang et al. 2022).

Various radical quenching experiments were further conducted utilizing radical scavengers. Ethanol (EtOH) was employed to scavenge both $\bullet\text{OH}$ ($K_{\text{OH}}=1.9\times 10^9\text{ M}^{-1}\text{ S}^{-1}$) and $\text{SO}_4^{\bullet-}$ ($K_{\text{SO}_4^{\bullet-}}=1.6\times 10^7\text{ M}^{-1}\text{ S}^{-1}$). Tert-butyl alcohol (TBA) was used as a typical quench agent for $\bullet\text{OH}$ ($K_{\text{OH}}=6.0\times 10^8\text{ M}^{-1}\text{ S}^{-1}$) (Wang et al. 2022c). As shown in Fig. S19a, the degradation efficiency of PCB28 dramatically decreased when 2 and 10 mM of EtOH were introduced into the Co-CGBC-700/PMS/PCB28 system, resulting in the removal of only 38.8% and 25.8% of PCB28, respectively, during 120 min reaction. However, the PCB28 degradation rate remained as high as 56.7% during the initial 10 min in the aqueous solution containing 2 mM TBA (Fig. 4i and S19b). Moreover, even with a TBA dosage of 10 mM, the removal rate was as high as 38%, outperforming that of EtOH as a radical scavenger. This indicated that the radical pathway involving $\text{SO}_4^{\bullet-}$ and $\bullet\text{OH}$ was significant, with $\text{SO}_4^{\bullet-}$ contributing predominantly to PCB28 degradation.

Furthermore, when 10 mM of furfuryl alcohol (FFA) (Fig. S19c), a unique scavenger for singlet oxygen, was introduced into the catalytic reaction, the degradation efficiency of PCB28 was significantly reduced. This demonstrates that the non-radical pathway involving $^1\text{O}_2$ was also crucial in the process of PCB28 degradation. As shown in Fig. S19d, 20 mM of NaI extremely inhibited the catalytic performance of Co-CGBC-700/PMS system for PCB28 degradation, further confirming that $\text{SO}_4^{\bullet-}$, $\bullet\text{OH}$ and $^1\text{O}_2$ were mainly generated via PMS activation on the catalyst surface, since I^- is also the strong quench agent for surface-bound free radicals (Wang et al. 2022c). As the impact of EtOH and TBA addition on BPA degradation was negligible (Fig. 4i, S19e and f), $^1\text{O}_2$ is the dominant ROS for BPA removal. Based on the above quenching experiments, both radical and non-radical

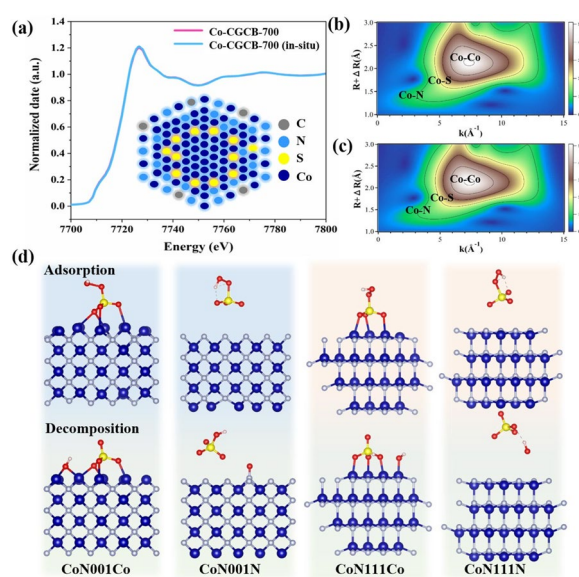


Fig. 5 **a** In-situ Co K-edge XANES of Co-CGBC-700 and **b,c** the corresponding WT-EXAFS plots of Co during the Fenton-like reaction. **(d)** DFT optimized geometries for adsorption of HSO_5^- and decomposition products onto the different CoN cluster surfaces of the prepared material, including both Co- and N-terminal surfaces of CoN(001) and CoN(111) facets. Color scheme: Co blue, N light blue, O red, C brown, S yellow and H grey

pathways played important roles in the degradation process of organic pollutants, where $\text{SO}_4^{\cdot-}$ and $\cdot\text{OH}$ and $^1\text{O}_2$ were dominant active species generated in the Co-CGBC-700/PMS system (Zhang et al. 2021). Thus, the degradation pathway of PCB28 was displayed in Text S5 and Fig. S20 and the generation of $^1\text{O}_2$ in this system facilitated phenolic compounds and reduced the toxicity of chlorinated organic formation.

To track the evolution of the atomic structure of Co during the catalytic process, we collected in situ XAFS spectra of Co-CGBC-700 in the presence of PMS. As depicted in Fig. 5a, the absorption edge was slightly shifted to a higher energy position compared with the pristine sample, indicating a decrease in the electron density of Co atoms. Moreover, the local environment evolution of Co was investigated by in situ EXAFS spectra (Fig. 5b, c and S21). The coordination numbers and the bond lengths remained almost the same during the AOPs, suggesting the overall structures also remained unchanged (Table S3). This would be the main reason, at the atomic level, for the excellent stability and cycling performance of the material. The *ex-situ* S K-edge NEXAFS of Co-CGBC-700 after the reaction further confirmed the stability of the NPCs (Fig. S22), and the increase in the peak at 2483 eV was attributed to the adsorption of SO_4^{2-} .

DFT calculations were further carried out to elucidate the role of the interfacial Co–N bonds in the binding of

PMS. Two preferential surfaces (001) and (111) with N or Co terminals were selected to compare the activation of HSO_5^- on various cubic CoN surfaces. Figure 5d shows DFT optimized adsorption geometries of reactant HSO_5^- and the corresponding products (OH^- and $\text{SO}_4^{\cdot-}$ radicals) on these surfaces. The reactant HSO_5^- was preferentially attached to three surface Co atoms in a tridentate conformation for Co-terminated surfaces, with average O–Co distances of 2.46 and 2.16 Å in CoN(001)-Co and CoN(111)-Co, respectively (Table S5). The N-terminated surfaces showed weak adsorption of HSO_5^- with O–N distances larger than 3.41 and 3.21 Å, for CoN(001)-N and CoN(111)-N, respectively. The stronger adsorption of PMS on Co-terminated surfaces caused larger elongation of the PMS O–O bond to 1.47 ~ 1.49 Å, thus favoring its bond cleavage. However, only the CoN(111)-Co surface showed an exothermic reaction energy of -2.27 eV, suggesting that it would be the most reactive surface that catalyzes the decomposition of HSO_5^- .

The calculated values of ΔE and the O–O bond demonstrated that the exposed CoN(111)-Co facet had a better capacity to activate HSO_5^- molecules. Moreover, the lengths of the O–Co bond and the HO-surface onto the CoN(111)-Co facet were 1.91 Å and 1.79 Å, which were shorter than those of other exposed facets, indicating that the most activated HSO_5^- molecules were tightly confined to form surface-reactive ROSs rather than being released into bulk solution. Together, due to the strong electronegativity and bridging effects of N atoms on the outer CoN surface of Co-NPCs anchored on biochar, electrons could be preferentially transferred from N and the substrate to the Co center, inducing highly efficient activation of PMS, which was consistent with the experimental results.

PCB28 degradation in natural water and soil (Text S1; Tables S6 and S7) was investigated. As presented in Fig. 6a, the degradation rates of PCB28 in natural water increased from 48.4% to 63.9% as the contaminant's concentration decreased from 2 to 1 mg L⁻¹, demonstrating the broad applicability of the Co-CGBC-700/PMS system for water remediation. The soil remediation in Fig. 6b shows that over 90% of PCB28 decomposed within 30 min in Co-CGBC-700/PMS system, while only ~25% of PCB28 can be eliminated by PMS alone. The leaching amount of Co ions was only 0.06 mg·L⁻¹, demonstrating that the as-prepared Co NPCs exhibited an excellent activity and ultra-stability for Fenton-like catalytic reactions to degrade a wide range of organic pollutants in natural environmental remediation (Fig. 6c).

Other 3d transitional mono-metal and bimetal NPCs were also prepared using the same strategy, including Ni, Cu and CoNi (Figs. S23 and S28; Tables S8 and S9). All of them exhibited the strong resistance against acid and

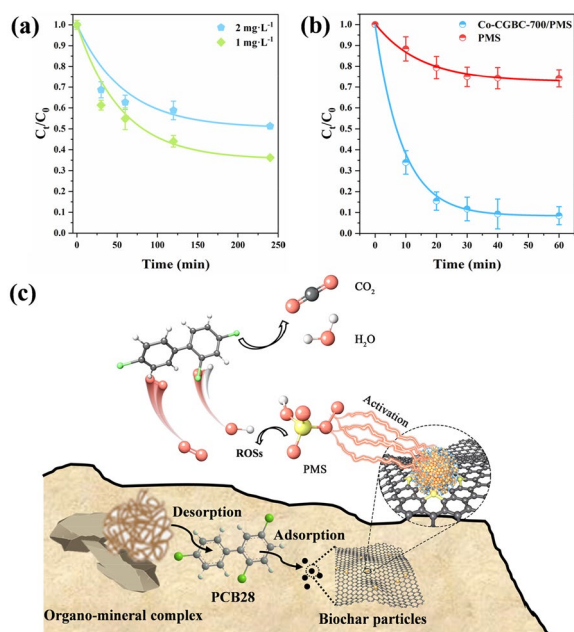


Fig. 6 **a** Different concentrations of PCB28 degradation in natural water (Xuanwu Lake, Nanjing), [catalyst] = 1.0 g·L⁻¹, [PMS] = 2 mM, pH = 6.5. **b** Catalytic activity for 50 mg·kg⁻¹ PCB28 degradation in natural soil (Yixing, Jiangsu province). [catalyst] = 15 mg, [soil] = 1 g, [PMS] = 10 mM, [PCB28] = 50 mg·kg⁻¹. **c** Diagram of PCB28 degradation process in Co-CGBC-700/PMS system in natural soil

aggregation, contributed from the core–shell structure and metal-support interaction. These findings show the feasibility of this cost-effective approach for developing 3d transition metal NPs with a radius of less than 10 nm and the potential applications in the environmental remediation, which will be reported in future work.

4 Conclusion

This work has demonstrated a general and efficient strategy to fabricate cost-effective 3d transition metal NPs via the pyrolysis of spent coffee grounds soaked in metal ions. The as-prepared Co NPs (Co-CGBC-700) exhibited an excellent activity and reusability for Fenton-like catalytic reactions to degrade a wide range of organic pollutants in environmental remediation. The resistance to acid and the decrease in binding energy of PMS are attributed to the coated CoN on the surface of metallic Co NPs. Moreover, the S-doped atoms enhanced the metal-support interaction and the adhesion strength at the metal-support interface, which eventually stabilized the NPs against aggregation by donating electrons to the active centers. These findings show the feasibility of this cost-effective approach for developing 3d transition metal NPs with a radius of less than 10 nm and the potential industrial applications in the environment remediation of organic pollution.

Supplementary Information

The online version contains supplementary material available at <https://doi.org/10.1007/s44246-024-00113-4>.

Supplementary Material 1.

Acknowledgements

The authors acknowledge the staff of beamline BL14W1 and BL11B at the Shanghai Synchrotron Radiation Facility (SSRF), 4B7A at the Beijing Synchrotron Radiation Facility (BSRF) and engineers of DEEP-INSPECTRA X1 from Beijing SCISTAR Co. Ltd. for their support in the XAS measurements.

Authors' contributions

All authors contributed to the study conception and design. Material preparation, data collection and analysis were performed by Y. Wang, P. Cui and Q. Yang. The first draft of the manuscript was written by Q. Yang, P. Cui and Y. Wang and all authors commented on previous versions of the manuscript. Q. Yang performed experiments helped with G. Fang and F. Dang. P. Cui, C. Liu and G. Fang performed XAFS measurements, data analysis, HAADF-STEM observation and DFT calculations. All the authors participated in analysis of the experimental data and discussions of the results. All authors read and approved the final manuscript.

Funding

This work was supported by the National Natural Science Foundation of China (42225701, 42022049, 42077145, 41701359), and the Natural Science Foundation of Jiangsu Province (BK20211400).

Availability of data and materials

Data will be made available on request.

Declarations

Competing interests

Shaobin Wang is an editor and Yujun Wang is an editorial board member for Carbon Research and were not involved in the editorial review, or the decision to publish this article. All authors declare that there are no competing interests.

Author details

¹State Key Laboratory of Soil and Sustainable Agriculture, Institute of Soil Science, Chinese Academy of Sciences, Nanjing 210008, P.R. China. ²University of Chinese Academy of Science, 100049 Beijing, P.R. China. ³Shanxi Metallurgical Geotechnical Engineering Investigation Co., Ltd, 030000 Taiyuan, P.R. China. ⁴School of Chemical Engineering and Advanced Materials, The University of Adelaide, North Terrace, Adelaide, SA 5005, Australia.

Received: 8 November 2023 Revised: 19 February 2024 Accepted: 14 March 2024

Published online: 06 April 2024

References

- Bao Y, Lian C, Huang K, Yu H, Liu W, Zhang J, Xing M (2022) Generating High-valent Iron-oxo $\equiv\text{FeIV}=\text{O}$ Complexes in Neutral Microenvironments through Peroxymonosulfate Activation by Zn–Fe Layered Double Hydroxides. *Angew Chem Int Ed Eng* 61(42):e202209542. <https://doi.org/10.1002/anie.202209542>
- Chen C, Ma T, Shang Y, Gao B, Jin B, Dan H, Li Q, Yue Q, Li Y, Wang Y, Xu X (2019) In-situ pyrolysis of Enteromorpha as carbocatalyst for catalytic removal of organic contaminants: Considering the intrinsic N/Fe in Enteromorpha and non-radical reaction. *Appl Catal B* 250:382–395. <https://doi.org/10.1016/j.apcatb.2019.03.048>
- Corma A, Concepción P, Boronat M, Sabater MJ, Navas J, Yacaman MJ, Larios E, Posadas A, López-Quintela MA, Buceta D, Mendoza E, Guilerá G, Mayoral A (2013) Exceptional oxidation activity with size-controlled supported

- gold clusters of low atomicity. *Nat Chem* 5(9):775–781. <https://doi.org/10.1038/nchem.1721>
- Cui P, Yang Q, Liu C, Wang Y, Fang G, Dionysiou DD, Wu T, Zhou Y, Ren J, Hou H, Wang Y (2021) An N, S-Anchored Single-Atom Catalyst Derived from Domestic Waste for Environmental Remediation. *ACS EST ENG* 1(10):1460–1469. <https://doi.org/10.1021/acsestengg.1c00255>
- Dai Y, Lu P, Cao Z, Campbell CT, Xia Y (2018) The physical chemistry and materials science behind sinter-resistant catalysts. *Chem Soc Rev* 47(12):4314–4331. <https://doi.org/10.1039/C7CS00650K>
- Duan X, Sun H, Wang S (2018) Metal-Free Carbocatalysis in Advanced Oxidation Reactions. *Acc Chem Res* 51(3):678–687. <https://doi.org/10.1021/acs.accounts.7b00535>
- Falcaro P, Ricco R, Yazdi A, Imaz I, Furukawa S, Maspoch D, Ameloot R, Evans JD, Doonan CJ (2016) Application of metal and metal oxide nanoparticles@MOFs. *Coord Chem Rev* 307:237–254. <https://doi.org/10.1016/j.ccr.2015.08.002>
- Fang G, Wu W, Liu C, Dionysiou DD, Deng Y, Zhou D (2017) Activation of persulfate with vanadium species for PCBs degradation: A mechanistic study. *Appl Catal B* 202:1–11. <https://doi.org/10.1016/j.apcatb.2016.09.006>
- Gao Y, Zhu Y, Chen Z, Hu C (2021) Nitrogen-Coordinated Cobalt Embedded in a Hollow Carbon Polyhedron for Superior Catalytic Oxidation of Organic Contaminants with Peroxymonosulfate. *ACS EST ENG* 1(1):76–85. <https://doi.org/10.1021/acsestengg.0c00039>
- Guo Y, Yuan P, Zhang J, Xia H, Cheng F, Zhou M, Li J, Qiao Y, Mu S, Xu Q (2018) Co₂P–CoN Double Active Centers Confined in N-Doped Carbon Nanotube: Heterostructural Engineering for Trifunctional Catalysis toward HER, ORR, OER, and Zn–Air Batteries Driven Water Splitting. *Adv Funct Mater* 28(51):1805641. <https://doi.org/10.1002/adfm.201805641>
- Guo ZY, Si Y, Xia WQ, Wang F, Liu HQ, Yang C, Zhang WJ, Li WW (2022) Electron delocalization triggers nonradical Fenton-like catalysis over spinel oxides. *Proc Natl Acad Sci* 119(31):e2201607119. <https://doi.org/10.1073/pnas.2201607119>
- Han H, Paik JW, Ham M, Kim KM, Park JK, Jeong YK (2020) Atomic Layer Deposition-Assisted Fabrication of Co-Nanoparticle/N-Doped Carbon Nanotube Hybrids as Efficient Electrocatalysts for the Oxygen Evolution Reaction. *Small* 16(33):2002427. <https://doi.org/10.1002/sml.2002427>
- Hansen TW, DeLaRiva AT, Challa SR, Datye AK (2013) Sintering of Catalytic Nanoparticles: Particle Migration or Ostwald Ripening? *Acc Chem Res* 46(8):1720–1730. <https://doi.org/10.1021/ar3002427>
- Hu S, Li WX (2021) Sabatier principle of metal-support interaction for design of ultrastable metal nanocatalysts. *Science* 374(6573):1360–1365. <https://doi.org/10.1126/science.abi9828>
- Jiang J, Zhao Z, Gao J, Li T, Li M, Zhou D, Dong S (2022) Nitrogen Vacancy-Modulated Peroxymonosulfate Nonradical Activation for Organic Contaminant Removal via High-Valent Cobalt-Oxo Species. *Environ Sci Technol* 56(9):5611–5619. <https://doi.org/10.1021/acs.est.2c01913>
- Jin H, Wang X, Tang C, Vasileff A, Li L, Slattey A, Qiao SZ (2021) Stable and Highly Efficient Hydrogen Evolution from Seawater Enabled by an Unsaturated Nickel Surface Nitride. *Adv Mater* 33(13):2007508. <https://doi.org/10.1002/adma.202007508>
- Joo SH, Park JY, Tsung CK, Yamada Y, Yang P, Somorjai GA (2009) Thermally stable Pt/mesoporous silica core–shell nanocatalysts for high-temperature reactions. *Nat Mater* 8(2):126–131. <https://doi.org/10.1038/nmat2329>
- Kigozi M, Kali R, Bello A, Padya B, Kalu-Uka GM, Wasswa J, Jain PK, Onwualu PA, Dzade NY (2020) Modified Activation Process for Supercapacitor Electrode Materials from African Maize Cob. *Materials* 13(23):5412. <https://doi.org/10.3390/ma13235412>
- Kilic MY, Abdelraheem WH, He X, Kestioglu K, Dionysiou DD (2019) Photochemical treatment of tyrosol, a model phenolic compound present in olive mill wastewater, by hydroxyl and sulfate radical-based advanced oxidation processes (AOPs). *J Hazard Mater* 367:734–742. <https://doi.org/10.1016/j.jhazmat.2018.06.062>
- Lei Y, Mehmood F, Lee S, Greeley J, Lee B, Seifert S, Winans RE, Elam JW, Meyer RJ, Redfern PC, Teschner D, Schlgöl R, Pellin MJ, Curtiss LA, Vajda S (2010) Increased Silver Activity for Direct Propylene Epoxidation via Subnanometer Size Effects. *Science* 328(5975):224–228. <https://doi.org/10.1126/science.1185200>
- Li X, Liu J, Rykov AI, Han H, Jin C, Liu X, Wang J (2015) Excellent photo-Fenton catalysts of Fe–Co Prussian blue analogues and their reaction mechanism study. *Appl Catal B* 179:196–205. <https://doi.org/10.1016/j.apcatb.2015.05.033>
- Li X, Huang X, Xi S, Miao S, Ding J, Cai W, Liu S, Yang X, Yang H, Gao J, Wang J, Huang Y, Zhang T, Liu B (2018) Single Cobalt Atoms Anchored on Porous N-Doped Graphene with Dual Reaction Sites for Efficient Fenton-like Catalysis. *J Am Chem Soc* 140(39):12469–12475. <https://doi.org/10.1021/jacs.8b05992>
- Li Z, Ji S, Liu Y, Cao X, Tian S, Chen Y, Niu Z, Li Y (2020) Well-Defined Materials for Heterogeneous Catalysis: From Nanoparticles to Isolated Single-Atom Sites. *Chem Rev* 120(2):623–682. <https://doi.org/10.1021/acs.chemrev.9b00311>
- Li M, Chen S, Jiang Q, Chen Q, Wang X, Yan Y, Liu J, Lv C, Ding W, Guo X (2021a) Origin of the Activity of Co–N–C Catalysts for Chemoselective Hydrogenation of Nitroarenes. *ACS Catal* 11(5):3026–3039. <https://doi.org/10.1021/acscatal.0c05479>
- Li N, Li R, Duan X, Yan B, Liu W, Cheng Z, Chen G, Hou L, Wang S (2021b) Correlation of Active Sites to Generated Reactive Species and Degradation Routes of Organics in Peroxymonosulfate Activation by Co-Loaded Carbon. *Environ Sci Technol* 55(23):16163–16174. <https://doi.org/10.1021/acs.est.1c06244>
- Liu L, Corma A (2018) Metal Catalysts for Heterogeneous Catalysis: From Single Atoms to Nanoclusters and Nanoparticles. *Chem Rev* 118(10):4981–5079. <https://doi.org/10.1021/acs.chemrev.7b00776>
- Moses K, Richard KK, Kingsley O, Ravi K, Omar LMK, Balaji P, Abdulhakeem B, Gabriel NK, Pawan KJ, John BK, Azikiwe PO, Nelson YD (2023) Porous carbon derived from Zea mays cobs as excellent electrodes for supercapacitor applications. *O J Anal Bioanal Chem* 7(1):001–010. <https://doi.org/10.17352/OJABC.000028>
- Ou H, Wang D, Li Y (2020) How to select effective electrocatalysts: Nano or single atom? *Nano Select*. 2(3):492–511. <https://doi.org/10.1002/nano.202000239>
- Roldan CB, Behafarid F (2015) Nanocatalysis: size- and shape-dependent chemisorption and catalytic reactivity. *Surf Sci Rep* 70(2):135–187. <https://doi.org/10.1016/j.surfrep.2015.01.001>
- Song F, Li W, Yang J, Han G, Yan T, Liu X, Rao Y, Liao P, Cao Z, Sun Y (2019) Interfacial Sites between Cobalt Nitride and Cobalt Act as Bifunctional Catalysts for Hydrogen Electrochemistry. *ACS Energy Lett* 4(7):1594–1601. <https://doi.org/10.1021/acsenergylett.9b00738>
- Tyo EC, Vajda S (2015) Catalysis by clusters with precise numbers of atoms. *Nat Nanotechnol* 10(7):577–588. <https://doi.org/10.1038/nnano.2015.140>
- van Deelen TW, Hernández Mejía C, de Jong KP (2019) Control of metal-support interactions in heterogeneous catalysts to enhance activity and selectivity. *Nat Catal* 2(11):955–970. <https://doi.org/10.1038/s41929-019-0364-x>
- Wang Q, Astruc D (2020) State of the Art and Prospects in Metal–Organic Framework (MOF)-Based and MOF-Derived Nanocatalysis. *Chem Rev* 120(2):1438–1511. <https://doi.org/10.1021/acs.chemrev.9b00223>
- Wang T, Wang M, Yang H, Xu M, Zuo C, Feng K, Xie M, Deng J, Zhong J, Zhou W, Cheng T, Li Y (2019) Weakening hydrogen adsorption on nickel via interstitial nitrogen doping promotes bifunctional hydrogen electrocatalysis in alkaline solution. *Energy Environ Sci*. 12(12):3522–3529. <https://doi.org/10.1039/C9EE01743G>
- Wang C, Wang Z, Mao S, Chen Z, Wang Y (2022a) Coordination environment of active sites and their effect on catalytic performance of heterogeneous catalysts. *Chinese J Catal* 43(4):928–955. [https://doi.org/10.1016/S1872-2067\(21\)63924-4](https://doi.org/10.1016/S1872-2067(21)63924-4)
- Wang L, Fu Y, Li Q, Wang Z (2022b) EPR Evidence for Mechanistic Diversity of Cu(II)/Peroxygen Oxidation Systems by Tracing the Origin of DMPO Spin Adducts. *Environ Sci Technol* 56(12):8796–8806. <https://doi.org/10.1021/acs.est.2c00459>
- Wang Z, Almatrafi E, Wang H, Qin H, Wang W, Du L, Chen S, Zeng G, Xu P (2022c) Cobalt Single Atoms Anchored on Oxygen-Doped Tubular Carbon Nitride for Efficient Peroxymonosulfate Activation: Simultaneous Coordination Structure and Morphology Modulation. *Angew Chem Int Ed* 61(29):e202202338. <https://doi.org/10.1002/ange.202202338>
- Wu T, Sun S, Song J, Xi S, Du Y, Chen B, Sasangka WA, Liao H, Gan CL, Scherer GG, Zeng L, Wang H, Li H, Grimaud A, Xu ZJ (2019) Iron-facilitated dynamic active-site generation on spinel CoAl₂O₄ with self-termination of surface reconstruction for water oxidation. *Nat Catal* 2(9):763–772. <https://doi.org/10.1038/s41929-019-0325-4>
- Wu L, Li B, Li Y, Fan X, Zhang F, Zhang G, Xia Q, Peng W (2021) Preferential Growth of the Cobalt (200) Facet in Co@N–C for Enhanced Performance in a Fenton-like Reaction. *ACS Catal* 11(9):5532–5543. <https://doi.org/10.1021/acscatal.1c00701>

- Xiong Y, Li H, Liu C, Zheng L, Liu C, Wang JO, Liu S, Han Y, Gu L, Qian J, Wang D (2022) Single-Atom Fe Catalysts for Fenton-Like Reactions: Roles of Different N Species. *Adv Mater* 34(17):2110653. <https://doi.org/10.1002/adma.202110653>
- Xu Z, Xiao FS, Purnell SK, Alexeev O, Kawi S, Deutsch SE, Gates BC (1994) Size-dependent catalytic activity of supported metal clusters. *Nature* 372(6504):346–348. <https://doi.org/10.1038/372346a0>
- Yang Y, Zeng R, Xiong Y, DiSalvo FJ, Abruña HD (2019) Cobalt-Based Nitride-Core Oxide-Shell Oxygen Reduction Electrocatalysts. *J Am Chem Soc* 141(49):19241–19245. <https://doi.org/10.1021/jacs.9b10809>
- Yang M, Hou Z, Zhang X, Gao B, Li Y, Shang Y, Yue Q, Duan X, Xu X (2022) Unveiling the Origins of Selective Oxidation in Single-Atom Catalysis via Co–N4–C Intensified Radical and Nonradical Pathways. *Environ Sci Technol* 56(16):11635–11645. <https://doi.org/10.1021/acs.est.2c01261>
- Yao Y, Wang C, Yan X, Zhang H, Xiao C, Qi J, Zhu Z, Zhou Y, Sun X, Duan X, Li J (2022) Rational Regulation of Co–N–C Coordination for High-Efficiency Generation of $^1\text{O}_2$ toward Nearly 100% Selective Degradation of Organic Pollutants. *Environ Sci Technol* 56(12):8833–8843. <https://doi.org/10.1021/acs.est.2c00706>
- Yin P, Luo X, Ma Y, Chu SQ, Chen S, Zheng X, Lu J, Wu XJ, Liang HW (2021) Sulfur stabilizing metal nanoclusters on carbon at high temperatures. *Nat Commun* 12(1):3135. <https://doi.org/10.1038/s41467-021-23426-z>
- Zhang LS, Jiang XH, Zhong ZA, Tian L, Sun Q, Cui YT, Lu X, Zou JP, Luo SL (2021) Carbon Nitride Supported High-Loading Fe Single-Atom Catalyst for Activation of Peroxymonosulfate to Generate $^1\text{O}_2$ with 100 % Selectivity. *Angew Chem Int Ed* 60(40):21751–21755. <https://doi.org/10.1002/anie.202109488>
- Zhang YJ, Huang GX, Winter LR, Chen JJ, Tian L, Mei SC, Zhang Z, Chen F, Guo ZY, Ji R, You YZ, Li WW, Liu XW, Yu HQ, Elimelech M (2022) Simultaneous nanocatalytic surface activation of pollutants and oxidants for highly efficient water decontamination. *Nat Commun* 13(1):3005. <https://doi.org/10.1002/ange.202202338>

Publisher's Note

Springer Nature remains neutral with regard to jurisdictional claims in published maps and institutional affiliations.